Mechanistic Study of Dry Reforming of Ethane by CO2 on a Bimetallic PtNi(111) Model Surface

Journal:	*Catalysis Science & Technology*
Manuscript ID	CY-ART-05-2018-000880.R1
Article Type:	Paper
Date Submitted by the Author:	07-Jun-2018
Complete List of Authors:	Kattel, Shyam; Brookhaven National Laboratory Chen, Jingguang; Columbia University, Chemical Engineering Liu, Ping; Brookhaven National Lab, Chemistry

Mechanistic Study of Dry Reforming of Ethane by CO_2 on a Bimetallic PtNi(111) Model Surface

Shyam Kattel[1], Jingguang G. Chen[1,2*] and Ping Liu[1*]

[1] *Chemistry Division, Brookhaven National Laboratory, Upton, New York 11973, United States*

[2] *Department of Chemical Engineering, Columbia University, New York, New York 10027, United States*

Corresponding Authors: jgchen@columbia.edu, pingliu3@bnl.gov

Abstract

Ethane (CH_3CH_3), one of the primary components of shale gas, is an attractive candidate for the production of syngas ($CO + H_2$) and ethylene (CH_2CH_2) via the selective C-C and C-H bond cleavage, respectively. Understanding the origin of the selective conversion is essential to design a good catalyst for CH_3CH_3 activation. Herein, we combined density functional theory (DFT) calculations with kinetic Monte Carlo (KMC) simulations to shed light on the mechanism of the oxidative C-H and C-C bond cleavage of CH_3CH_3 on a PtNi(111) model catalyst using CO_2 as an oxidant, where the estimated selectivity is in good agreement with the experimental results on PtNi nanoparticles supported on CeO_2. Our calculations show that PtNi is selective to CO via direct CO_2 dissociation and the oxidative C-C bond scission of CH_3CH_3 via the oxygenated ($*C_2H_yO$) intermediates. By comparison the CH_2CH_2 selectivity via the selective C-H bond scission of $*CH_3CH_3$, is much lower. The kinetic analysis suggests that the selectivity of PtNi toward syngas can be enhanced by facilitating the formation of key $*C_2H_yO$ intermediates; while the selectivity toward CH_2CH_2 is promoted mainly by accelerating the C-H bond scission of $*CH_3CH_2$ to produce $*CH_2CH_2$.

Keywords: Ethane dry reforming; CO_2 activation; PtNi alloy; DFT; KMC; Mechanism.

1. Introduction

Ethane (CH_3CH_3) is one of the primary components of shale gas.[1] The large reserve of shale gas makes CH_3CH_3 an attractive candidate for its use as a feedstock chemical. Dry reforming of CH_3CH_3 using one of the greenhouse gases, [2, 3] CO_2, as an oxidant[4-7] has gained significant interests recently.[8-14] The reaction can occur via two distinct pathways: (1) the C-C bond cleavage of CH_3CH_3 (i. e. the reforming reaction) to produce synthesis gas (syngas: CO + H_2), precursors for the production of long-chain hydrocarbons by the Fischer-Tropsch synthesis[15, 16], and (2) oxidative C-H bond cleavage of CH_3CH_3 (i. e. the oxidative dehydrogenation reaction) to produce ethylene (CH_2CH_2 + CO + H_2O),[12, 17, 18], an important building block in chemical industry for the production of chemicals such as polyethylene, ethylene oxide, styrene, acetaldehyde, vinyl acetate, ethanol, and ethylbenzene, etc.[19] The production of CH_2CH_2 via the oxidative dehydrogenation of CH_3CH_3 occurs at lower temperatures (400 - 600 °C), and therefore more beneficial [19-21] than the currently used thermal dehydrogenation, which requires elevated temperatures (750-950 °C). Thus, the design of catalysts that selectively promote either C-C or C-H bond cleavage of CH_3CH_3 is desirable, but remained challenging due to the lack of detailed understanding on the kinetics of such complex reaction network.

Under the conditions of CH_3CH_3 dry reforming using CO_2, bimetallic PtNi and PtCo catalysts supported on CeO_2 ($PtNi/CeO_2$ and $PtCo/CeO_2$ in our notation) were shown previously to promote the oxidative C-C bond cleavage of CH_3CH_3 to produce syngas while $FeNi/CeO_2$ catalysts favored the oxidative C-H bond cleavage to produce CH_2CH_2.[22] According to the thermodynamic studies using density functional theory (DFT) calculations on the selective steps involved in this process, the C-C bond cleavage was preferred on Pt(111), PtCo(111) [12] and

PtNi(111) [13] model surfaces while the C-H bond cleavage was favored on NiFe(111). [22] Yet, the mechanistic understanding required for the design of selective catalysts for CH_3CH_3 dry reforming is limited, as the complete reaction network and the reaction kinetics still remain unknown.

In the current study, DFT calculations are coupled with kinetic Monte Carlo (KMC) simulations to establish the complete reaction network and describe the reaction kinetics for the conversion of CH_3CH_3 to CH_2CH_2 and syngas on the PtNi(111) bimetallic model surface, being able to well describe the experimentally measured selectivity of PtNi nanoparticles supported on CeO_2 under similar reaction conditions. [13] To our best knowledge, this is a first detailed theoretical investigation and the first study being able to establish the complex reaction network of CO_2 reduction by ethane and provide in-depth mechanistic understanding of the oxidative C-H and C-C bond cleavage of ethane. It also allows us to identify the key factors that control the selectivity. The results suggest that there are two important steps among the complex reaction network, which are essential to the overall conversion and selectivity. One is the C-O bond scission of CO_2 to form *CO and *O. It is more favorable than the competing hydrogenation reactions to form carboxylate (*COOH) or formate (*HCOO) species because of the lack surface *H. The other is the formation of $*C_2H_xO$ intermediates due to oxidation of C_2H_x by surface *O.[12, 22] The C-C bond scission of $*C_2H_xO$ intermediates finally leads to the formation of syngas. The high selectivity toward syngas estimated theoretically as well as observed experimentally depends on the capability of PtNi alloy in promoting C-O bond formation between $*C_2H_y$ intermediates and *O and producing the critical $*C_2H_yO$ intermediates to facilitate the C-C bond cleavage. The selectivity toward CH_2CH_2 can be promoted by facilitating the two successive C-H bond scission of $*CH_3CH_3$.

2. Computational Methods

2.1 Density Functional Theory (DFT) Calculations

Spin polarized density functional theory (DFT)[23, 24] calculations were performed using the Vienna *Ab-Initio* Simulation Package (VASP) code.[25, 26] Projector augmented wave (PAW)[27] potentials were used to describe the core electrons with the generalized gradient approximation (GGA) using PW91 functionals. The Kohn-Sham one-electron wave functions were expanded by using a plane wave basis set with a kinetic energy cutoff of 400 eV. The Brillouin zone was sampled using a 3 × 3 × 1 k-point grid in the Monkhorst-Pack[28] scheme. Ionic positions were optimized until Hellman-Feynman force on each ion was smaller than 0.02 eV/Å.

A near surface alloy motif, Pt/Ni/Pt(111) or PtNi(111) in our notation, was used to model the PtNi alloy surface, where the subsurface (the 2nd layer) of Pt(111) was replaced by Ni atoms. In our previous experimental studies, we have determined, based on the characteristic vibrational frequencies of CO adsorption using Fourier-transform infrared spectroscopy (FTIR), that PtNi bimetallic particles prefer the Pt surface termination.[13] This is also consistent with the DFT prediction of favorable Pt segregation to the surface of PtNi(111).[29, 30] Such model is to represent the favorable segregation near the surface of PtNi alloy, which results in a Pt-enriched surface and Ni-enriched subsurface layers.[31] Furthermore, PtNi(111) model was used previously, being able to successfully describe the performances of Pt-based bimetallic catalysts during various catalytic hydrogenation reactions.[32, 33] Indeed, for CO_2 reduction by CH_3CH_3 (see Section 3.2), it is able to describe well the selectivity of PtNi/CeO_2 reported experimentally, based on combined DFT and KMC simulations under similar reaction conditions. The bimetallic surface was modeled using a four layer 3 × 3 surface slab. A 14 Å thick vacuum was added along the direction perpendicular to the surface in the initial slab model to avoid the artificial interactions

between the slab and its periodic images. During geometry optimization, the atoms in the bottom two layers were fixed, while all other atoms were allowed to relax. The binding energy (BE) of an adsorbate is calculated as

$$BE(adsorbate) = E(slab + adsorbate) - E(slab) - E(adsorbate)$$

where E(slab + adsorbate), E(slab) and E(adsorbate) are the total energies of slab with adsorbate, clean slab, and adsorbate species in gas phase, respectively.

The transition state of a chemical reaction was located using the climbing image nudged elastic band (CI-NEB) method implemented in VASP.[34] The activation energy (E_a) of a chemical reaction is defined as the energy difference between the initial and transition states while the reaction energy (ΔE) is defined as the energy difference between the initial and final states.

2.2 Kinetic Monte Carlo (KMC) Simulations

The kinetic Monte Carlo (KMC) simulations were performed with a Kinetix module implemented in Materials Studio 5.5.[35] The details about the implementation of the KMC method is provided in ref [35]. The present KMC simulations were carried out at reaction conditions in previous experiments: ratio of partial pressure of CO_2 and CH_3CH_3 (P_{CO2}/P_{CH3CH3}) = 2:1 and temperature (T) = 873 K.[13] The surface chemical reactions were modeled on a 128 × 128 matrix. For simplicity, each atop site represents a surface site in the KMC simulations.

The reaction rates were computed based on calculated reaction barriers using the Arrhenius equation given by $A_0\exp(-E_a/k_BT)$. E_a is the activation energy of the corresponding reaction obtained from DFT calculations, k_B is the Boltzmann constant and T is the temperature of the KMC simulations. For the reactions involving molecules in the gas-phase, the contribution from the entropy was taken from the NIST database[36] and was included in the KMC simulations.

The adsorption coefficient was calculated according to $PA_{site}\sigma/\sqrt{2\pi m k_B T}$ 37, where P, A_{site}, σ and m represent the pressure of the adsorbed gas, the area of a single site, the sticking coefficient and the mass of the adsorption gas, respectively. A_0 is the prefactor. A gas phase prefactor of 1.0 $\times 10^{13}$ s^{-1} was used for all surface reactions.

3. Results and Discussion

3.1 DFT Results

The DFT calculations were performed to obtain ΔE and E_a of 89 elementary reaction steps relevant to possible pathways for dry reforming of CH_3CH_3 by CO_2 on the PtNi(111) surface. Depending on the products, the reaction can be grouped into two pathways: (1) production of CH_2CH_2 via the oxidative C-H bond cleavage pathway (Figure 1); (2) production of syngas via the C-C bond cleavage pathway (Figures 2 and 3). The formation of methanol (CH_3OH) and methane (CH_4) was also included as possible side products (Figure 4).

3.1.1 Activation of CO_2

The activation of CO_2 is one of the key steps for dry reforming of CH_3CH_3 by CO_2, which produces CO and provides *O species as oxidizing agent for CH_3CH_3 oxidation. CO_2 is physisorbed on PtNi(111) (BE = -0.04 eV). The direct *CO_2 dissociation to *CO + *O is a potentially difficult step (ΔE = 1.52 eV and E_a = 2.13 eV, Table S3). By comparison, in the presence of *H dissociated from *CH_3CH_3, *CO_2 prefers to undergo the reverse-water-gas-shift (RWGS) reaction to form *HOCO (ΔE = 0.23 eV, E_a = 1.02 eV) or *HCOO (ΔE = 0.40 eV, E_a = 1.33 eV) intermediate with lower barriers according to the DFT calculated barriers. Here

*HOCO is an active intermediate on PtNi(111), as reported for Pt(111) [38], which leads to the formation of *CO and hydroxyl (*OH) species (ΔE = 0.69 eV, E_a = 0.83 eV). The surface *O is generated preferentially via the *OH dissociation (ΔE = 0.62 eV, E_a = 1.40 eV) in this case which can be reduced back to *OH (ΔE = -0.62 eV; E_a = 0.78 eV) and eventually *H_2O (ΔE = -1.08 eV; E_a = 0.31 eV), or help the C-H bond cleavage via the formation of *H_2O. Yet, as will be seen in section 3.2 the KMC simulations indicate that the direct CO_2 dissociation to *C and *C is dominant under reaction conditions and is essential to the overall conversion and selectivity toward syngas. By comparison, the dissociation of *CO to *C and *O is rather difficult with very large activation energy (ΔE = 2.94 eV; E_a = 4.09 eV) and is thus unlikely to occur. Therefore this reaction was not included in the DFT and KMC analysis of the reaction network for oxidative C-H and C-C bond cleavage of ethane.

3.1.2 Dehydrogenation of CH_3CH_3 to CH_2CH_2

The dehydrogenation of CH_3CH_3 to CH_2CH_2 is the only path way leading toward the production and therefore controlling the selectivity of CH_2CH_2 during the dry reforming of CH_3CH_3 by CO_2. The binding of CH_3CH_3 on PtNi(111) is weak with the BE of -0.05 eV (Table S1) due to the high stability of the molecule. Consequently, the first C-H bond scission of *CH_3CH_3 is rather difficult (ΔE = 0.57 eV; E_a = 1.12 eV), though it is feasible at the typical experimental reaction temperature of ~873 K.[13] The dissociated *CH_3CH_2 is strongly bound on the surface (BE = -1.62 eV) and undergoes the second C-H bond scission, which produces either *CH_3CH (ΔE = 0.61 eV; E_a = 1.21 eV) or *CH_2CH_2 (ΔE = 0.33 eV; E_a = 1.06 eV). Once *CH_2CH_2 is formed, desorption (BE = -0.54 eV) is preferred over the C-H bond cleavage to *CH_2CH (ΔE = 0.71 eV, E_a = 1.21 eV). The third C-H bond scission favors the formation of

CH_3C (ΔE = -0.34 eV, E_a = 0.53 eV), yet the further dehydrogenations successively toCH_2C, *CHC and *CC are much more difficult (E_a > 1.4 eV, Table S2).

Alternatively, *O can assist the dehydrogenations of *CH_3CH_3, via the concerted step *CH_3CH_3 + *O → *CH_3CH_2 + *OH (ΔE = 0.01 eV, E_a = 1.39 eV) and *CH_3CH_2 + *O → *CH_2CH_2 + *OH (ΔE = -0.31 eV; E_a = 1.26 eV). The dissociated *O fragment in this case forms *H_2O via its two sequential hydrogenation reactions (*O + *H → *OH + * and *O + *OH → *H_2O + *). Thus, the presence of *O can help to sequester atomic *H. On the other hand, *O can also participate directly in the oxidation of the *C_2H_y intermediates to facilitate the C-C bond scission, as discussed below. However, both O-assisted dehydrogenation steps are more difficult than the corresponding direct dehydrogenation discussed above. Therefore, the direct dehydrogenation of *CH_3CH_3 is likely the pathway to produce CH_2CH_2 on PtNi(111).

3.1.3 Oxidation of C_2H_x to C_2H_xO intermediates and syngas

The oxidation of C_2H_x for the production of C_2H_xO intermediates is essential to promote the C-C bond cleavage and therefore the production of syngas. Figures 2 and 3 summarize the reaction networks for the oxidative C-C bond cleavage of CH_3CH_3 with CO_2 as an oxidant to produce syngas. The initial step for the oxidative C-C bond cleavage, similar to the pathways for the oxidative C-H bond cleavage, is the formation of *CH_3CH_2 and *O intermediates. The reforming of CH_3CH_3 by CO_2 to syngas may occur via the C-C bond scission of *C_2H_y intermediates formed from *CH_3CH_3 dehydrogenation as demonstrated in Section 3.1.1.

The DFT results (Figure 2 and Table S4) show that the C-C bond scissions of *CH_3CH_2 (ΔE = 1.01 eV, E_a = 2.38 eV), *CH_3CH (ΔE = 0.35 eV, E_a = 1.46), *CH_2CH_2 (ΔE = 1.44 eV, E_a = 2.18), *CH_3C (ΔE = 1.31 eV, E_a = 2.03), *CH_2CH (ΔE = 0.79 eV, E_a = 1.67), *CHCH (ΔE =

0.38 eV, E_a = 1.74), *CH_2C (ΔE = 1.27 eV, E_a = 2.71),*CHC (ΔE = 0.06 eV, E_a = 1.35) and *CC intermediates (ΔE = 0.07 eV, E_a = 1.32 eV) are rather difficult on PtNi(111) and can be hindered kinetically. Alternatively, in the presence of *O from *OH and/or *CO_2 dissociation, the oxidations of *C_2H_y to *C_2H_yO likely occur preferentially over the C-C bond scission, which may facilitate the formation of *CO via the C-H and/or C-C bond scissions. Indeed, the oxidations and formations of *CH_3CH_2O (ΔE = -0.72 eV, E_a = 1.08 eV), *CH_3CHO (ΔE = -1.58 eV, E_a = 1.20 eV), *CH_3CO (ΔE = -1.57 eV, E_a = 1.16 eV), *CH_2CH_2O (ΔE = -0.39 eV, E_a = 0.64 eV), *CH_2CHO (ΔE = -1.42 eV, E_a = 1.16 eV), *CH_2CO (ΔE = -1.82 eV, E_a = 0.99 eV), *CHCHO (ΔE = -1.49 eV, E_a = 0.14 eV), *CHCO (ΔE = -2.50 eV, E_a = 1.06 eV) and *CCO (ΔE = -3.46 eV, E_a = 1.41 eV) intermediates are more favorable than the corresponding C-C bond scissions to produce *CH_y species (Table S5). According to the DFT calculations, there are two possible ways for the formation of syngas. One starts with the *CH_3CH_2O intermediate from *CH_3CH_2 oxidation, which is followed by the sequential dehydrogenations to *CCO (blue highlights, Figure 2). The *CCO intermediate enables the C-C bond cleavage and therefore the formations of *CO and *C (ΔE = 0.10 eV, E_a = 0.81 eV), where *C is subsequently oxidized to *CO by the *O species (ΔE = -2.94 eV, E_a = 1.15 eV). Along the other pathway (blue highlights, Figure 3 and Tables S2 and S4), the production of syngas starts with dehydrogenation of *CH_3CH_2 to *CH_3CH or *CH_2CH_2 as that shown in section 3.1.1. Both intermediates lead to the common *CH_2CO species via oxidation and dehydrogenation reactions. Eventually, *CO is formed either via C-H bond cleavage of *CH_2CO to *CCO and C-C bond cleavage of *CCO, or via C-C bond breaking of *CH_2CO, where the dissociated *CH_2 is then converted to CO via *CH (ΔE = -0.04 eV, E_a = 0.55 eV), *CHO (ΔE = -1.55 eV, E_a =1.04 eV) and *CO (ΔE = -0.55

eV, E_a = 0.50 eV) intermediates. The two paths are energetically comparable according to the DFT-calculated barriers, and may run in parallel for the production of CO.

3.1.4 Hydrogenation of CO to CH_3OH and CH_4

Previously it has been reported that Pt-based catalysts convert CO_2 selectively to CO or CH_4 upon reactions with H_2 or CH_3CH_3.[12, 39, 40] Therefore, *CO here was considered as the possible source for CH_3OH production. Due to the strong Pt-CO interaction (BE = -1.27 eV, Table S1), the desorption of *CO to gas phase is hindered; instead, the reactions with *H from CH_3CH_3 decomposition to form *CHO (ΔE = 0.55 eV, E_a = 0.95 eV), *CH_2O (ΔE = 0.34 eV, E_a = 0.72 eV), *CH_3O (ΔE = -0.08 eV, E_a = 0.06 eV) and eventually *CH_3OH (ΔE = -0.98 eV, E_a = 0.25 eV) are more favorable (Figure 4a and Table S3). The hydrogenation of *C from *CCO dissociation produces CH_4 via *CH (ΔE = -0.75 eV, E_a = 0.63 eV), *CH_2 (ΔE = 0.04 eV, E_a = 0.59 eV), *CH_3 (ΔE = -0.67 eV, E_a = 0.44 eV) and *CH_4 (ΔE = -0.61 eV, E_a = 1.86 eV) intermediates (Figure 4b and Table S3); by comparison, the oxidation of *C to *CO (ΔE = -2.94 eV, E_a = 1.15 eV) is less favorable.

Overall, according to the DFT-calculated activation barriers the most favorable pathway to produce CH_2CH_2 on PtNi(111) is via two successive but selective C-H bond cleavage of *CH_3CH_3 (highlighted in blue, Figure 1). The formation of syngas occurs via the formation of *CH_3CH_2, *CH_3CH/*CH_2CH_2/*CH_3CH_2O, *CH_3C/*CH_2CH_2O/*CH_3CHO, *CH_3CO/*CH_2CHO and *CH_2CO intermediates (highlighted in blue, Figure 2 and 3). It is noted that *CH_2CO is a common reaction intermediate in all DFT-predicted pathways for the C-C bond cleavage of CH_3CH_3, and a key precursor leading to the formation of *CO via the direct C-C bond scission.

During the reaction, PtNi(111) is able to provide selective binding motifs and energies to the reaction intermediates. All the C_xH_y species are bound to the surface via the unsaturated C atoms (Figure 5). This is also the case for some of the C_xH_yO species (Figure 6), including *CO, *HCO, *H_3CO, *CCO, *CHCO, *CH_2CO, *CH_3CO, *CH_2CHO, *CH_3CHO and *CH_3CH_2O. For the others, e.g. *H_2CO, *CCH_2O, *$CHCH_2O$ and *CH_2CH_2, the interaction is through C and O atoms on two adjacent surface sites. The *OH_x species bind with PtNi(111) only via O at hollow, bridge or top sites (Figure 7). According to the DFT calculated binding energies (Table S1), PtNi(111) is able to provide strong binding to most of *C_xH_y, *C_xH_yO and *OH_x species, while it is selectively inactive toward *CH_2CH_2, *CH_2O, *CH_2CO, *CH_3CHO and *H_2O intermediates.

3.2 KMC results

Although the DFT calculations have addressed the energetics for CH_3CH_3 reforming by CO_2 on PtNi(111), the effect on the reaction kinetics remains elusive. What is the selectivity of PtNi(111) toward syngas and CH_2CH_2 under the reaction conditions? Which are the dominant pathways and reaction intermediates? What are the key kinetic parameters or descriptors that control the activity and selectivity? To answer these questions, KMC simulations followed by a sensitivity analysis were conducted. The KMC simulations were performed at typical experimental reaction conditions (see Section 2.2) by including 91 elementary reactions leading to the productions of CH_2CH_2 and syngas as well as CH_4 and CH_3OH.

3.2.1 Selectivity

Figure 8a shows the formation rate of H_2, H_2O, CH_2CH_2 and CO obtained from the KMC simulations. On PtNi(111) the dominant pathway for CH_3CH_3 reforming by CO_2 is the

production of CO. The corresponding selectivity is ~54%, which is estimated according to rate[CO] / (rate[CO] + rate[C_2H_4] + rate[H_2O] + rate[H_2]). Here, rate[CO], rate[C_2H_4], rate[H_2O] and rate[H_2] are the steady state rate of CO, C_2H_4, H_2O and H_2 formation, respectively, in the KMC simulations. The major contribution to the production of CO is from CO_2 via the direct dissociation and/or the RWGS reaction; in contrast the CO selectivity resulting from the C-C bond scission of *CH_3CH_3 is found to be lower (32 %). The KMC simulation results reveal that the rate for *CO_2 dissociation to *CO is much higher than the rate for *HOCO formation and dissociation (Figure S3), though the preference should be opposite according to the barriers from DFT calculations in section 3.1. The formations of CH_4 and CH_3OH are not observed in the KMC simulations, indicating that the *CO intermediate formed during the reaction prefers to desorb rather than being hydrogenated to CH_4 or CH_3OH.

The observed selectivity can be well described according to the coverage of various surface species observed in the KMC simulations. The main surface species identified from the KMC results (Figure 8b) are *C, *O and *OH, where the coverage of *C and *OH are very low (< 10%) and that for *O is also less than 40%. That is, the surface is only partially oxidized under the reaction condition. This is consistent with our previous experimental results on $PtNi/CeO_2$. [13] The presence of *O as a surface intermediate suggests that direct *CO_2 dissociation to *CO + *O is plausible, rather than hydrogenation to *HOCO. Furthermore, the presence of *C as a surface intermediate suggests that the CO formation, among many possible pathways, occurs via the C-C bond scission predominantly from *CCO, *CHCO, *CH_2CO*CHC, and *CC. The lack of *H species on the surface favors CO_2 dissociation over hydrogenation, and therefore the partial oxidation on PtNi(111). At the high temperature in the KMC simulations, the *H species on the surface are not stable and likely desorb as H_2 (Figure

8). As a result, the *CO_2 hydrogenation to *HOCO, which corresponds to a lower barriers than that of the *CO_2 dissociation according to DFT calculations, is not as favorable as CO_2 dissociation kinetically. Our results highlight that the kinetic modeling under reaction conditions is essential to describe such complex reaction networks appropriately. However, these surface species do not poison the catalyst but rather act as active intermediates or precursors for the steady formation of the products: H_2, H_2O, CH_2CH_2 and CO.

3.2.2 Dominant pathways

The rates obtained from the KMC simulations were used to determine the dominant reaction channels that lead to the various products under reaction conditions. According to rate of each elementary step (Figures S1-S5), the formation of *CH_2CH_2 primarily occurs via two successive direct C-H bond scission reactions of *CH_3CH_3 (Figures 9 and S1), consistent with the DFT hypothesis in section 3.1. A small amount of *CH_2CH_2 is observed via the *O assisted dehydrogenation of *CH_3CH_3 (Figure S1), where *O species act as *H acceptors to form *H_2O, similarly to the role of lattice oxygen in oxide-based catalysts.[41-43] *CH_2CH_2 is then desorbed as a product. The dehydrogenation of *CH_2CH_2 to *CH_2CH is not observed from the KMC simulations and only a small amount of *CH_2CH_2 reacts with *O to form *CH_2CH_2O (Figures 7a and S5), which eventually produces CO via the C-C bond scission. It is observed that ~95% CH_2CH_2 is desorbed as a product since *CH_2CH_2 is weakly bound on PtNi(111).

Different from the hypothesis merely according to the DFT-calculated barriers, the synthesis of syngas does not solely prefer the path via the oxidation of *C_2H_y intermediates and the common *CH_2CO intermediate (Figures 2 and 3). The KMC results show that this is the case in term of the dominate path for the conversion to CO (Figure 9). The path starts with the

oxidation of *CH_3CH_2 to an oxygenated *CH_3CH_2O intermediate (Figure S5). The *CH_3CH_2O intermediate then undergoes three successive C-H bond scission steps to form *CH_2CO, which subsequently follows the path leading to the formation of *CO via *CHCO. There are two rate-comparable paths for *CHCO to react (Figures S2 and S4). One is the C-C bond scission to produce *CH and *CO, where *CH is then converted to *CO via *CHO; the other involves the C-H bond scission to *CCO, which is followed by the C-C bond cleavage to form *C and *CO intermediates.

In addition, the KMC simulations also identify a new path, not predicted in the DFT calculations, contributed to CO production. Along the new path, the sequential C-H bond scission reactions of *CH_3CH_3 lead to the formation of *CC via the intermediates: *CH_3CH_2, *CH_3CH, *CH_3C, *CH_2C and *CHC (Figure 9). The C-C bond cleavage of *CHC and *CC occurs to form *C, which reacts with *O and forms *CO (Figure S4). Alternatively *CH_3C (Figure 9) can be oxidized to *CH_3CO by *O. (Figure S5). Both steps are comparable in rate (Figures S1 and S5). *CH_3CO undergoes two successive C-H bond scissions to form *CHCO (Figure S4). The KMC results show that the combined rate for the direct and *O assisted dehydrogenation of *CH_3CH_2 to *CH_2CH_2 (Figure S1) is ~3 times higher than that of *CH_3CH_2O formation from *O insertion reaction of *CH_3CH_2 (Figure S5). However, the sequential steps leading to the formation of *CO are more activated than those along the dominant pathway.

Overall, the results show that KMC simulations provide a more accurate and complete description of such complex reaction network than the DFT calculations alone, being able to identify not only the active source for *O species different from that expected using DFT, but also the new routes for CO production in addition to the favorable pathways predicted from the

DFT calculations. The KMC analysis suggests that the most dominant pathway for the formation of CO occurs via $*CH_3CH_2 \rightarrow *CH_3CH_2O \rightarrow *CH_3CHO \rightarrow *CH_3CO \rightarrow *CH_2CO \rightarrow *CHCO \rightarrow *CH+*CO/*CCO \rightarrow *C + *CO$ (Figure 9). The C-C bond scission is mainly promoted when $*C_2H_yO$ intermediates are formed, consistent with the mechanism suggested on NiO based catalysts.[44] By comparison, the contribution from the direct C-C bond scission of $*C_2H_y$ species to the overall CO production is very small, only via the dissociation of *CHC and *CC intermediates (Figure S4). Therefore, the formation of the $*C_2H_yO$ intermediates ($*C_2H_y + *O \rightarrow *C_2H_yO$) is essential for the selective C-C bond cleavage of CH_3CH_3 to produce syngas.

3.3 Key descriptors

Using the KMC model, the sensitivity analysis was performed to identify the selectivity-controlling steps and the corresponding descriptors for PtNi(111) for the reaction of CH_3CH_3 with CO_2. The sensitivity analysis was carried out by shifting the E_a of each elementary step by a small amount from its original value and keeping the other parameters constant, which was successfully used to identify descriptors to control catalytic performance in previous studies.[45, 46] Our results show that the CH_2CH_2 selectivity on PtNi is more sensitive to the formation of $*CH_2CH_2$. As shown in Figure 10a, a slight promotion to the C-H bond scission of $*CH_3CH_2$ can result in a significant increase in CH_2CH_2 production. The suppression of $*CH_2CH_2$ desorption from PtNi(111) lowers the CH_2CH_2 selectivity (Figure 10a), but enhancing the syngas selectivity (Figure 10b). When $*CH_2CH_2$ is strongly bound, desorption is hindered, while the oxidation to form $*CH_2CH_2O$ and syngas formation via the C-C bond cleavage are promoted during the activation of CH_3CH_3. Following the same idea, the hindered formation $*CH_2CH_2$ from $*CH_3CH_2$ also helps in syngas selectivity (Figure 10b), which tunes the reaction of $*CH_3CH_2$ toward formation of $*CH_3CH_2O$, a key intermediate for CO production as indicated above.

Besides, *O insertion reactions of *CH_3CH_2 to *CH_3CH_2O and *CH_2CH_2 to *CH_2CH_2O are also important to the syngas production, and promoting the formations of *CH_3CH_2O and *CH_2CH_2O can facilitate the oxidative C-C bond cleavage of CH_3CH_3 to produce syngas (Figure 10b).

According to the sensitivity analysis, the enhanced CH_2CH_2 selectivity primarily depends on a facilitated dehydrogenation of *CH_3CH_2. To increase the selectivity toward syngas, the reaction between *CH_3CH_2 and *O to form the critical *CH_3CH_2O intermediate is essential. Improving the syngas selectivity depends on bindings of *CH_3CH_2/*CH_2CH_2 and *O intermediates, which should be strong enough to allow a reasonable amount of the species present on the surface, but weak enough to enable the oxidation reaction to occur. Our study suggests that *O binding energy is a potential descriptor that affects the key steps leading to different products during CH_3CH_3 reforming by CO_2. The weakened *O binding on PtNi can hinder the CO production from *CO_2 dissociation, a significant contribution for CO selectivity according to the KMC simulations. Furthermore, it may result simultaneously in a hindered syngas production due to the decreased amount of *O species on the surface necessary for the oxidation of C_2H_x intermediates as well as an enhanced syngas production via the facilitated oxidative C-C bond cleavage of CH_3CH_3, and vice versa for the strengthened *O binding. In addition, the complete oxidation and the deactivation of the PtNi catalyst may occur if the *O is over-stabilized. A small tuning in *O binding on the PtNi catalyst can affect several key steps involved in the CH_3CH_3 reforming by CO_2 and consequently the catalytic performance.

4. Conclusions

The DFT calculations were combined with the KMC simulations to shed light on the mechanisms of the oxidative C-H and C-C bond cleavage of CH_3CH_3 to produce CH_2CH_2 and

syngas, respectively on the bimetallic PtNi(111) model surface using CO_2 as an oxidant. Here, the KMC simulations were performed at typical experimental reaction conditions, including not only the elementary steps to produce CH_2CH_2, CO and H_2, but also those leading to the formation of CH_4 and CH_3OH. The results show that the production of CH_2CH_2 occurs via two successive but selective C-H bond scission reactions of $*CH_3CH_3$. To produce syngas from CH_3CH_3 activation, $*CH_3CH_3$ primarily undergoes the C-C bond scission of $*C_2H_yO$ intermediates produced via the C-H bond scission and *O insertion reactions of $*C_2H_y$ species. In contrast, the contribution from the direct C-C bond scission of C_2H_y species is very small. The direct dissociation of $*CO_2$ is also important, which is the primary source for CO and provides *O species to facilitate the formation of $*C_2H_yO$ intermediates for syngas production.

Based on the DFT results on PtNi(111), the KMC simulations are able to well describe the high CO or syngas selectivity of PtNi nanoparticles supported on CeO_2 reported observed experimentally. During this process, the formation of $*C_2H_yO$ intermediates is essential for the C-C bond cleavage and therefore syngas production, which can be further enhanced by facilitating the reaction between $*C_2H_y$ and *O via either increasing the amount of both species or lowering the barriers for *O insertion. By comparison the lower CH_2CH_2 selectivity can be increased primarily when the C-H bond scission of $*CH_3CH_2$ to produce $*CH_2CH_2$ is promoted. Our study not only provides the mechanistic understandings of such complex reactions, but also enables the identification of key descriptors to potentially tune the catalytic selectivity, where the combination of DFT calculations and KMC simulations is essential to well describe the complex reaction kinetics.

Acknowledgments

The research was carried out at Brookhaven National Laboratory (BNL) supported by the U.S. Department of Energy (DOE), Office of Science, Office of Basic Energy Sciences, Division of Chemical Sciences, Biosciences and Geosciences, under contract DE-SC0012704. The DFT calculations were performed using computational resources at the Center for Functional Nanomaterials at BNL, a DOE Office of Science User Facility, and at the National Energy Research Scientific Computing Center (NERSC), a DOE Office of Science User Facility, supported by the Office of Science of the DOE under contract DE-AC02-05CH11231.

References

1. N. Mimura, I. Takahara, M. Inaba, M. Okamoto and K. Murata, *Catal Commun*, 2002, **3**, 257-262.
2. J. Hansen, M. Sato, R. Ruedy, K. Lo, D. W. Lea and M. Medina-Elizade, *P Natl Acad Sci USA*, 2006, **103**, 14288-14293.
3. T. R. Knutson and R. E. Tuleya, *J Climate*, 2004, **17**, 3477-3495.
4. M. M. Nair and S. Kaliaguine, *New J Chem*, 2016, **40**, 4049-4060.
5. L. Shi, G. H. Yang, K. Tao, Y. Yoneyama, Y. S. Tan and N. Tsubaki, *Accounts Chem Res*, 2013, **46**, 1838-1847.
6. M. Usman, W. M. A. W. Daud and H. F. Abbas, *Renew Sust Energ Rev*, 2015, **45**, 710-744.
7. D. Pakhare and J. Spivey, *Chem Soc Rev*, 2014, **43**, 7813-7837.
8. R. Koirala, R. Buechel, S. E. Pratsinis and A. Baiker, *Appl Catal a-Gen*, 2016, **527**, 96-108.
9. A. Toth, G. Halasi and F. Solymosi, *J Catal*, 2015, **330**, 1-5.
10. T. Baidya, N. van Vegten and A. Baiker, *Top Catal*, 2011, **54**, 881-887.
11. S. Deng, S. G. Li, H. Q. Li and Y. Zhang, *Ind Eng Chem Res*, 2009, **48**, 7561-7566.
12. M. D. Porosoff, M. N. Z. Myint, S. Kattel, Z. H. Xie, E. Gomez, P. Liu and J. G. G. Chen, *Angew Chem Int Edit*, 2015, **54**, 15501-15505.
13. B. H. Yan, X. F. Yang, S. Y. Yao, J. Wan, M. Myint, E. Gomez, Z. H. Xie, S. Kattel, W. Q. Xu and J. G. G. Chen, *Acs Catal*, 2016, **6**, 7283-7292.
14. J. Q. Zhu, S. Qin, S. T. Ren, X. X. Peng, D. M. Tong and C. W. Hu, *Catal Today*, 2009, **148**, 310-315.
15. I. Wender, *Fuel Process Technol*, 1996, **48**, 189-297.
16. D. J. Wilhelm, D. R. Simbeck, A. D. Karp and R. L. Dickenson, *Fuel Process Technol*, 2001, **71**, 139-148.
17. D. Melzer, P. H. Xu, D. Hartmann, Y. Y. Zhu, N. D. Browning, M. Sanchez-Sanchez and J. A. Lercher, *Angew Chem Int Edit*, 2016, **55**, 8873-8877.

18. H. B. Zhu, D. C. Rosenfeld, M. Harb, D. H. Anjum, M. N. Hedhili, S. Ould-Chikh and J. M. Basset, *Acs Catal*, 2016, **6**, 2852-2866.
19. R. Koirala, R. Buechel, F. Krumeich, S. E. Pratsinis and A. Baiker, *Acs Catal*, 2015, **5**, 690-702.
20. C. A. Gartner, A. C. van Veen and J. A. Lercher, *Chemcatchem*, 2013, **5**, 3196-3217.
21. F. Cavani, N. Ballarini and A. Cericola, *Catal Today*, 2007, **127**, 113-131.
22. M. Myint, B. H. Yan, J. Wan, S. Zhao and J. G. G. Chen, *J Catal*, 2016, **343**, 168-177.
23. P. Hohenberg and W. Kohn, *Phys Rev B*, 1964, **136**, B864-+.
24. W. Kohn and L. J. Sham, *Phys Rev*, 1965, **140**, 1133-&.
25. G. Kresse and J. Furthmuller, *Comp Mater Sci*, 1996, **6**, 15-50.
26. G. Kresse and J. Furthmuller, *Phys Rev B*, 1996, **54**, 11169-11186.
27. P. E. Blochl, *Phys Rev B*, 1994, **50**, 17953-17979.
28. H. J. Monkhorst and J. D. Pack, *Phys Rev B*, 1976, **13**, 5188-5192.
29. A. V. Ruban, H. L. Skriver and J. K. Norskov, *Phys Rev B*, 1999, **59**, 15990-16000.
30. A. U. Nilekar, A. V. Ruban and M. Mavrikakis, *Surf Sci*, 2009, **603**, 91-96.
31. J. R. Kitchin, J. K. Norskov, M. A. Barteau and J. G. Chen, *J Chem Phys*, 2004, **120**, 10240-10246.
32. Z. Y. Duan and G. F. Wang, *Phys Chem Chem Phys*, 2011, **13**, 20178-20187.
33. J. A. Herron and M. Mavrikakis, *Catal Commun*, 2014, **52**, 65-71.
34. G. Henkelman, B. P. Uberuaga and H. Jonsson, *J Chem Phys*, 2000, **113**, 9901-9904.
35. J. J. Lukkien, J. P. L. Segers, P. A. J. Hilbers, R. J. Gelten and A. P. J. Jansen, *Phys Rev E*, 1998, **58**, 2598-2610.
36. http://cccbdb.nist.gov
37. A. P. J. Jansen, An introduction to Monte Carlo simulations of surface reactions. (Springer-Verlag Berlin Heidelberg, 2012).
38. L. C. Grabow, A. A. Gokhale, S. T. Evans, J. A. Dumesic and M. Mavrikakis, *J Phys Chem C*, 2008, **112**, 4608-4617.
39. M. D. Porosoff and J. G. G. Chen, *J Catal*, 2013, **301**, 30-37.
40. S. Kattel, B. H. Yan, J. G. G. Chen and P. Liu, *J Catal*, 2016, **343**, 115-126.
41. B. Solsona, P. Concepcion, S. Hernandez, B. Demicol and J. M. L. Nieto, *Catal Today*, 2012, **180**, 51-58.
42. G. L. Dai, Z. P. Liu, W. N. Wang, J. Lu and K. N. Fan, *J Phys Chem C*, 2008, **112**, 3719-3725.
43. V. Fung, F. Tao and D. E. Jiang, *Catal Sci Technol*, 2016, **6**, 6861-6869.
44. Z. Skoufa, E. Heracleous and A. A. Lemonidou, *J Catal*, 2015, **322**, 118-129.
45. S. Kattel, B. H. Yan, Y. X. Yang, J. G. G. Chen and P. Liu, *J Am Chem Soc*, 2016, **138**, 12440-12450.
46. Y. X. Yang, M. G. White and P. Liu, *J Phys Chem C*, 2012, **116**, 248-256.

Figures and Captions

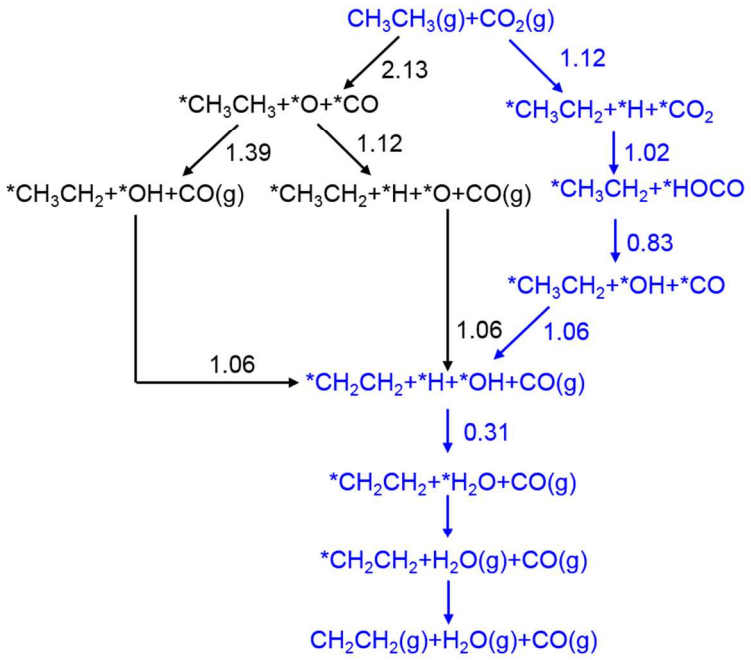

Figure 1. Reaction pathways for the oxidative CH_3CH_3 dehydrogenation to CH_2CH_2. Numbers adjacent to arrows represent E_a (in eV) for the corresponding elementary reactions. The DFT predicted most favorable pathways for CH_2CH_2(g) formation are highlighted in blue.

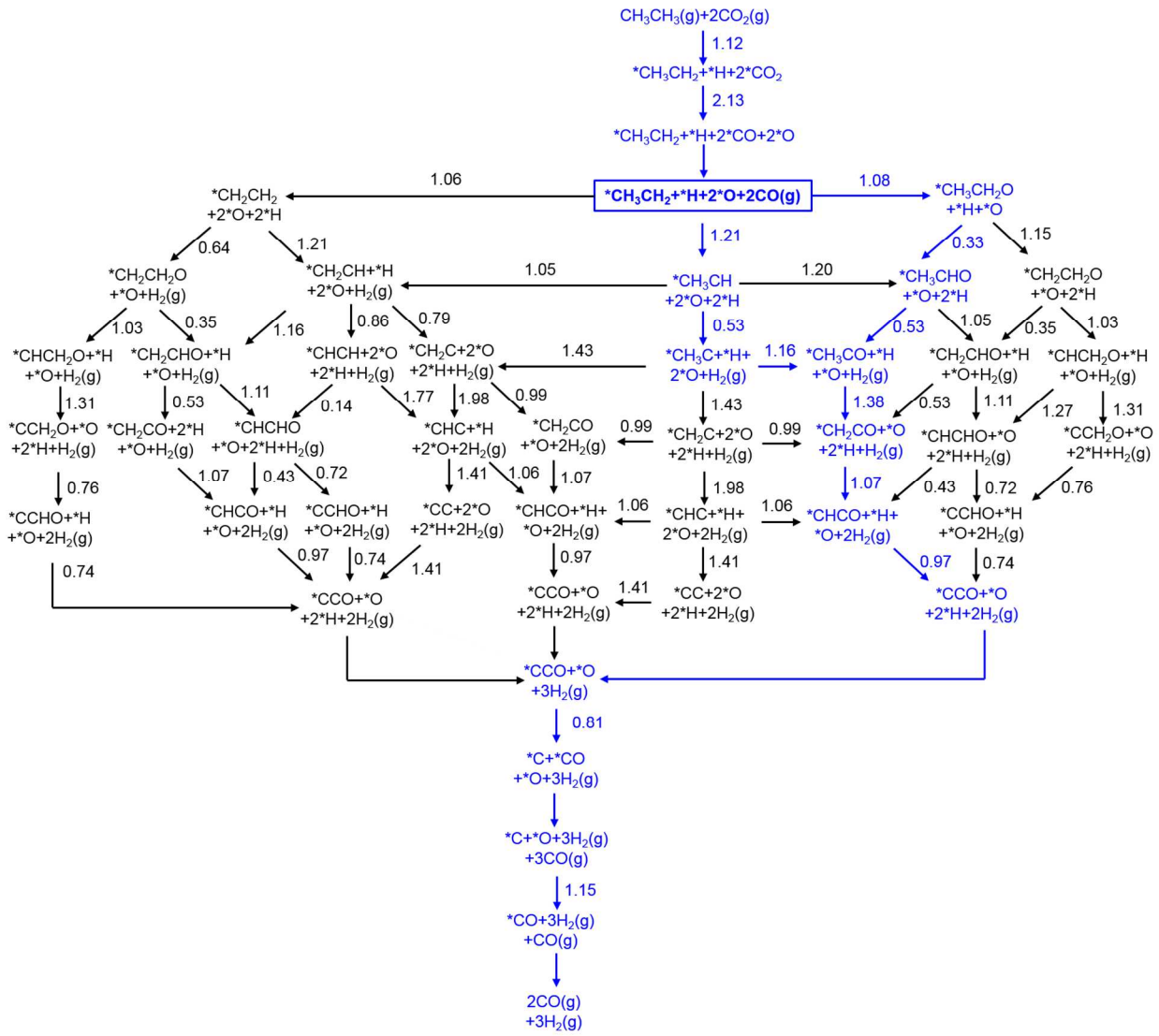

Figure 2. Reaction pathways for the oxidative C-C bond cleavage of CH_3CH_3 to produce CO + H_2. Along the reaction pathways, $*CH_3CH_2$ produced due to the initial C-H bond scission of CH_3CH_3 leads to the formation of $*C_xH_y$ and $*C_xH_yO$ species due C-H bond scission and *O insertion reactions. $*C_xH_y$ and $*C_xH_yO$ species undergo C-H bond scission and *O insertion reactions to form a common *CCO intermediate which finally undergoes C-C bond scission reaction. For simplicity, 2CO(g) produced due to $*CO_2$ dissociation (3rd step in this reaction mechanisms) is omitted in rest of the reaction steps. Numbers adjacent to arrows represent E_a (in eV) for the corresponding elementary reactions. The DFT predicted most favorable pathways for C-C bond scission of CH_3CH_3 to produce CO(g) are highlighted in blue.

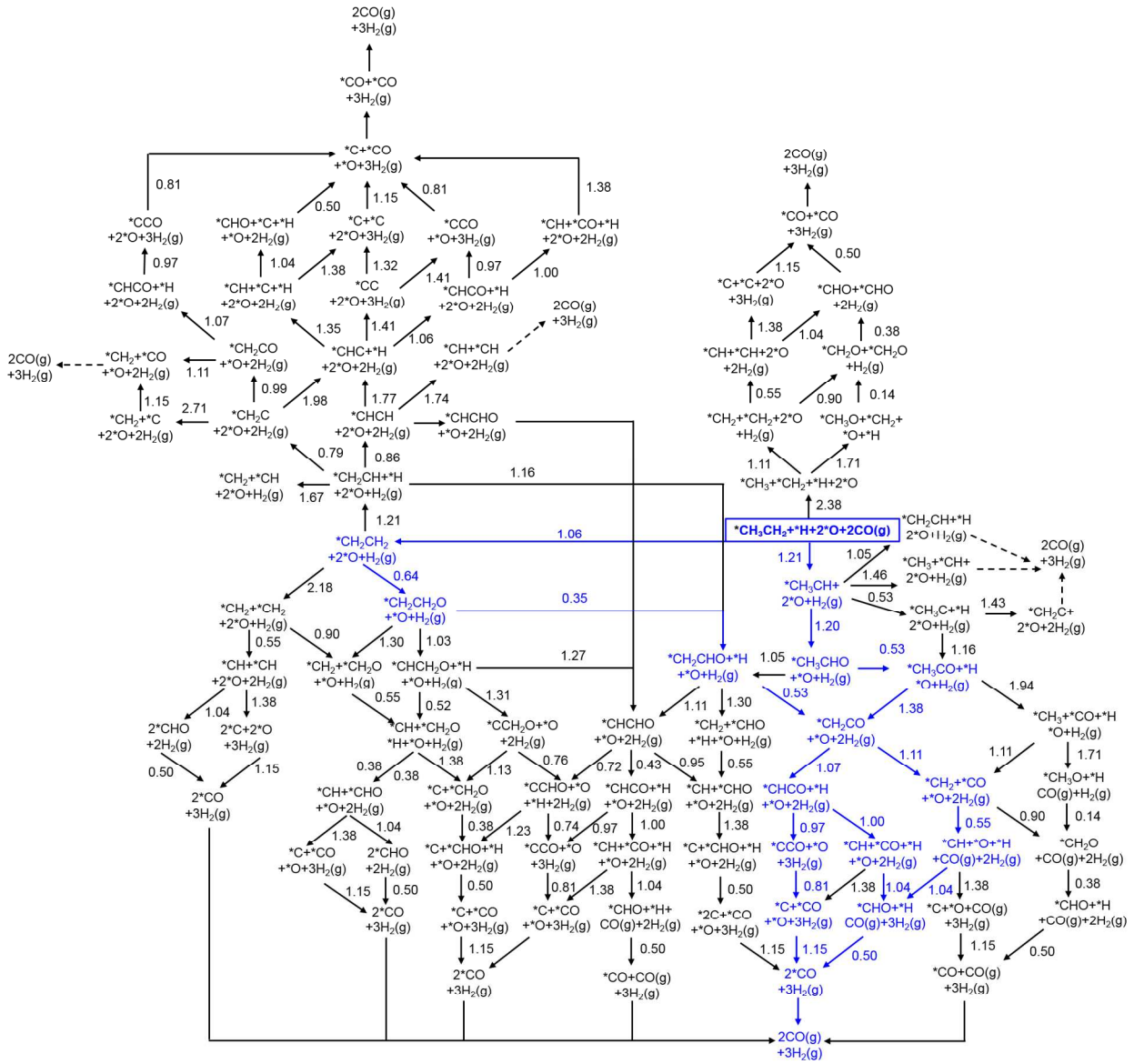

Figure 3. Reaction pathways for the oxidative C-C bond cleavage of CH_3CH_3 to produce CO + H_2. Along the reaction pathways, CO formation via the direct the C-C bond scission of $*C_xH_y$ and $*C_xH_yO$ species were included. For simplicity, the reaction was assumed to be started from $*CH_3CH_2$ + *H + 2*O+ 2CO(g) (3rd step in reaction mechanism shown in Figure 2) and 2CO(g) was omitted in rest of the reaction steps. Numbers adjacent to arrows represent E_a (in eV) for the corresponding elementary reactions. The DFT predicted most favorable pathways for C-C bond scission of CH_3CH_3 to produce CO(g) are highlighted in blue. The dashed arrows only show the final products without the intermediates steps since these pathways are replicas and do not add new routes for the formation of the products. For simplicity two elementary reactions for H_2 desorption are not shown explicitly here. As shown in Figure 2, H_2 desorption reaction always consists of two elementary reactions: $*C_2H_x/*C_2H_xO$ + * → $*C_2H_{x-1}/*C_2H_{x-1}O$ + *H and *H + *H → H_2(g) + 2*.

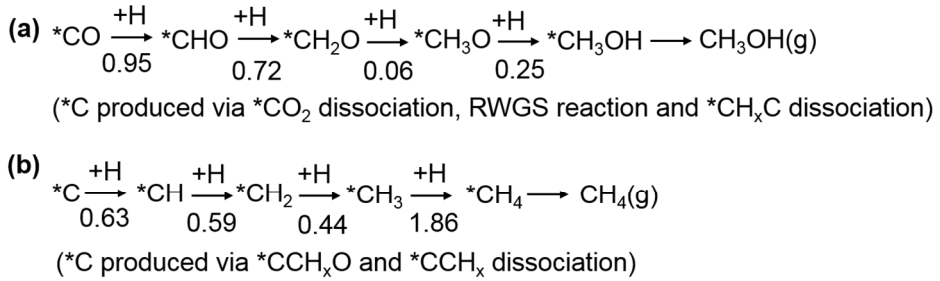

Figure 4. Pathways for the formation of $CH_3OH(g)$ and $CH_4(g)$. Numbers adjacent to arrows represent E_a (in eV) for the corresponding elementary reactions.

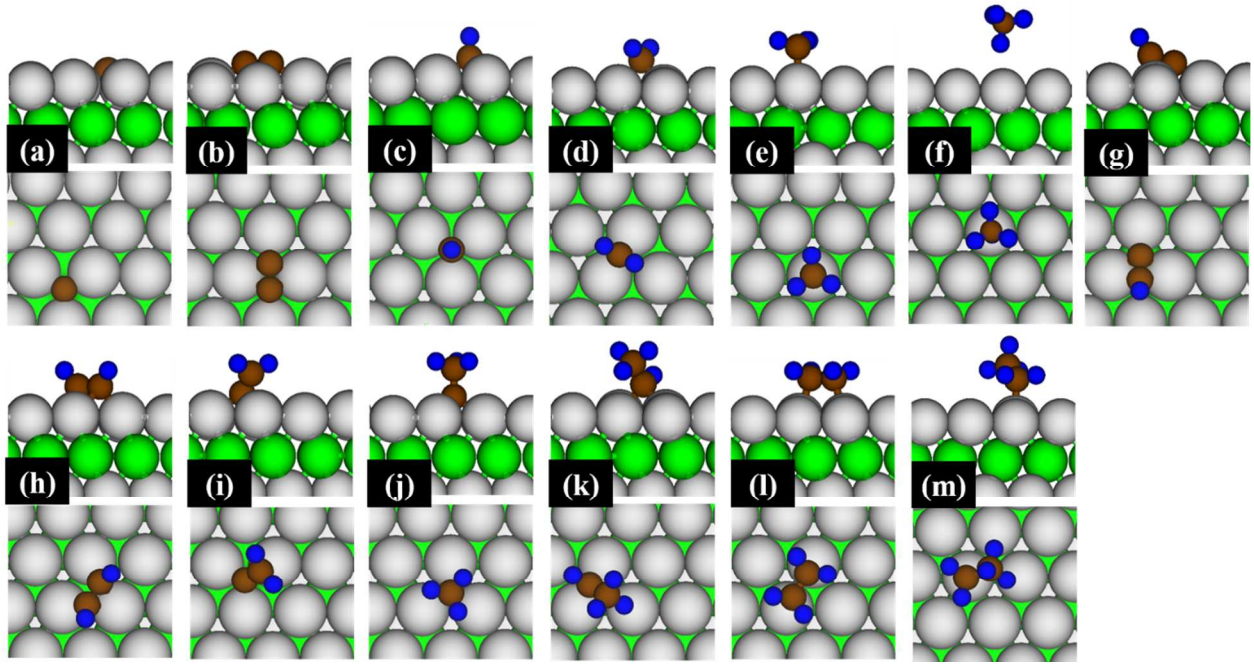

Figure 5. Side and top views of optimized geometries of (a) *C, (b) *CC, (c) *CH, (d) *CH_2, (e) *CH_3, (f) *CH_4, (g) *CCH, (h) *CHCH (i) *CH_2C (j) *CH_3C (k) *CH_3CH, (l) *CH_2CH_2 and (m) *CH_3CH_2 on the PtNi(111) surface. * = adsorbed species. Pt: grey, Ni: green, C: brown and H: blue.

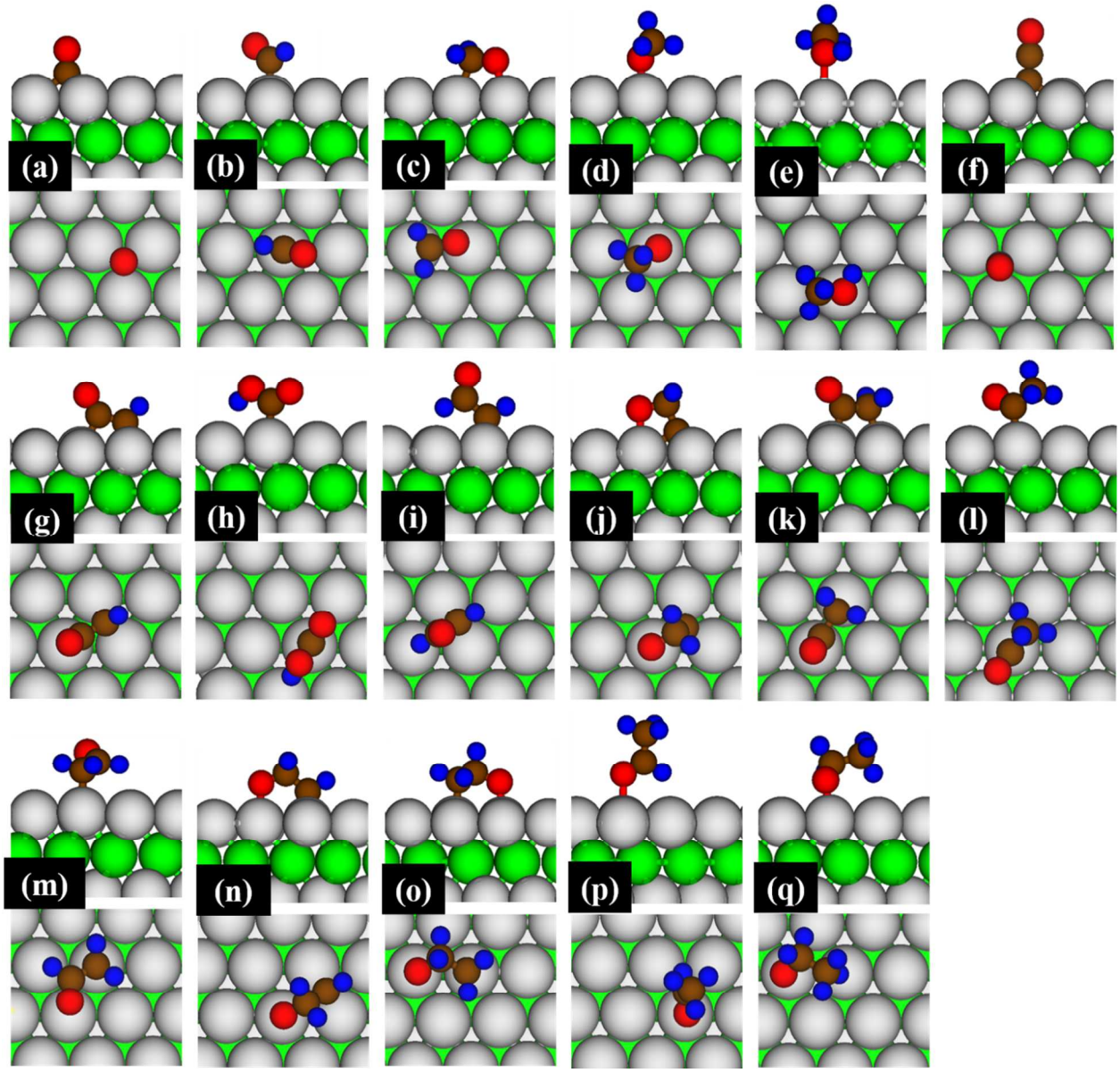

Figure 6. Side and top views of optimized geometries of (a) *CO, (b) *CHO, (c) *CH_2O, (d) *CH_3O (e) *CH_3OH, (f) *CCO, (g) *CHCO, (h) *HOCO (i) *CHCHO (j) *CCH_2O (k) *CH_2CO, (l) *CH_3CO, (m) *CH_2CHO, (n) *$CHCH_2O$, (o) CH_2CH_2O, (p) *CH_3CHO and (q) *CH_3CH_2O on the PtNi(111) surface. * = adsorbed species. Pt: grey, Ni: green, O: red, C: brown and H: blue.

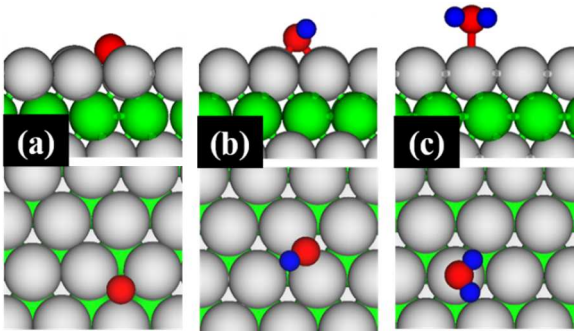

Figure 7. Side and top views of optimized geometries of (a) *O, (b) *OH and (c) *H_2O on the PtNi(111) surface. * = adsorbed species. Pt: grey, Ni: green, O: red and H: blue.

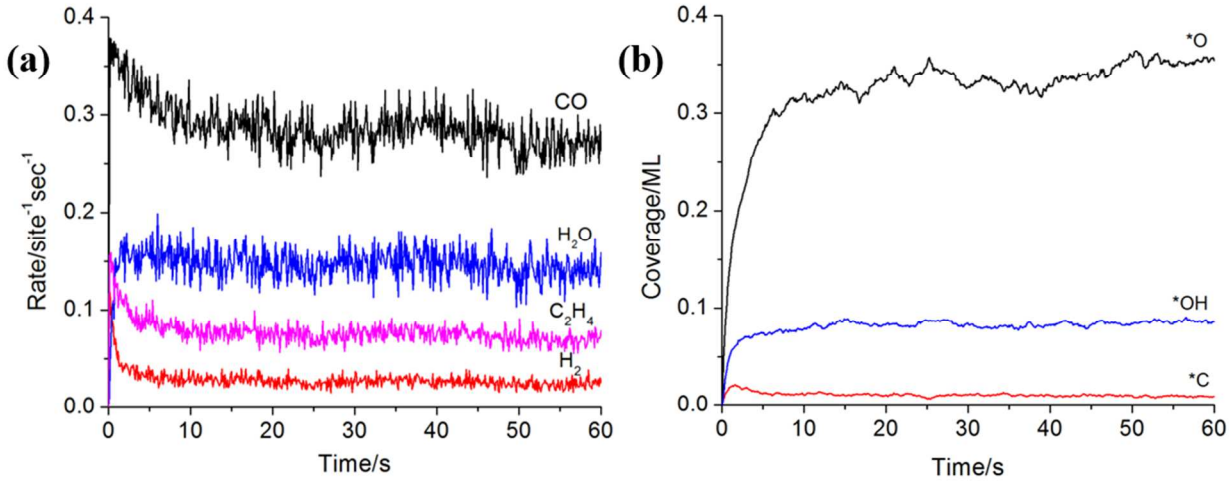

Figure 8. KMC results. (a) The rate of formation of products: H_2, H_2O, CH_2CH_2 and CO and (b) the coverage of surface species *C, *O and *OH.

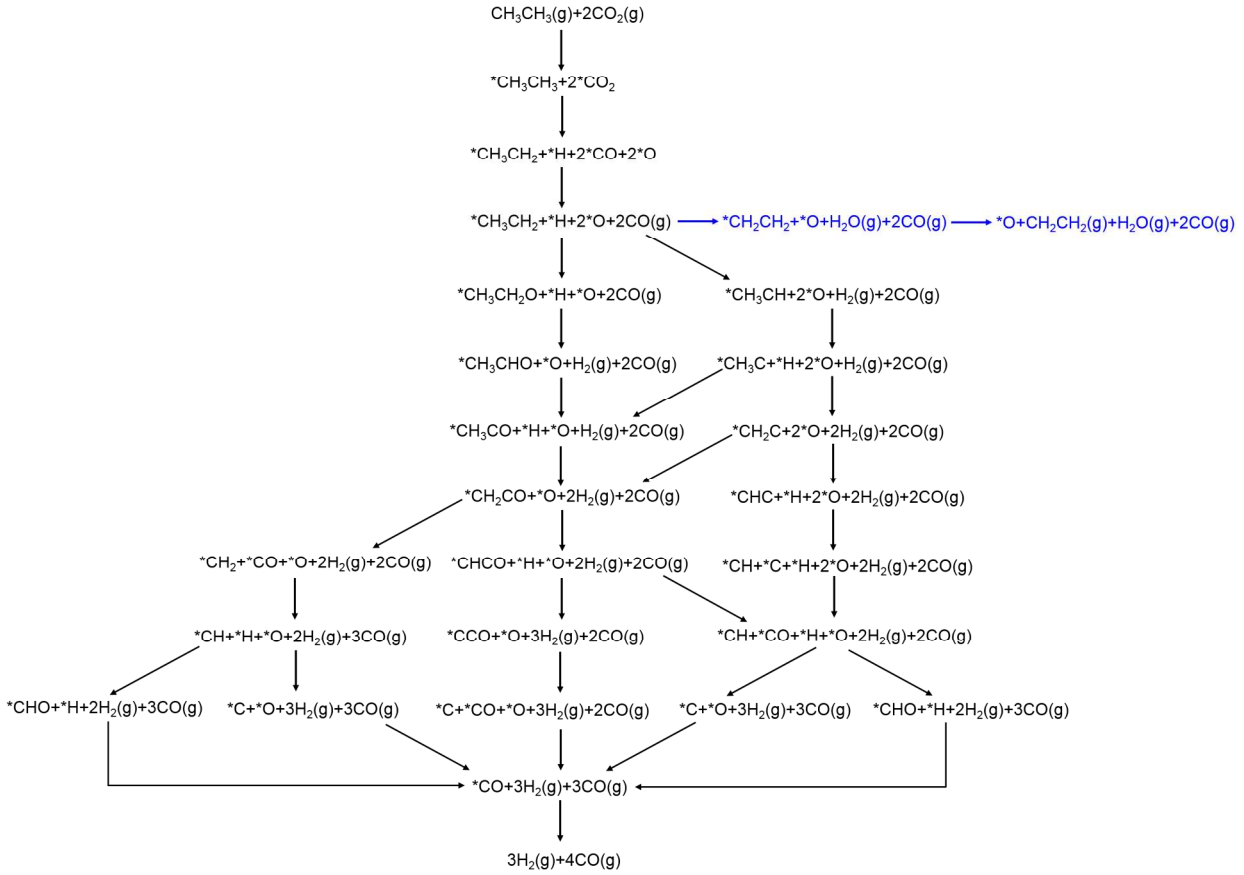

Figure 9. KMC predicted pathways the oxidative C-H and C-C bond cleavage of $*CH_3CH_3$ to produce CH_2CH_2 and CO + H_2. The preferred pathways for the production of CH_2CH_2(g) and syngas were shown in blue and black, respectively. For simplicity two elementary reactions for H_2 desorption are not shown explicitly here. As shown in Figure 2, H_2 desorption reaction always consists of two elementary reactions: $*C_2H_x/*C_2H_xO + * \rightarrow *C_2H_{x-1}/*C_2H_{x-1}O + *H$ and $*H + *H \rightarrow H_2(g) + 2*$.

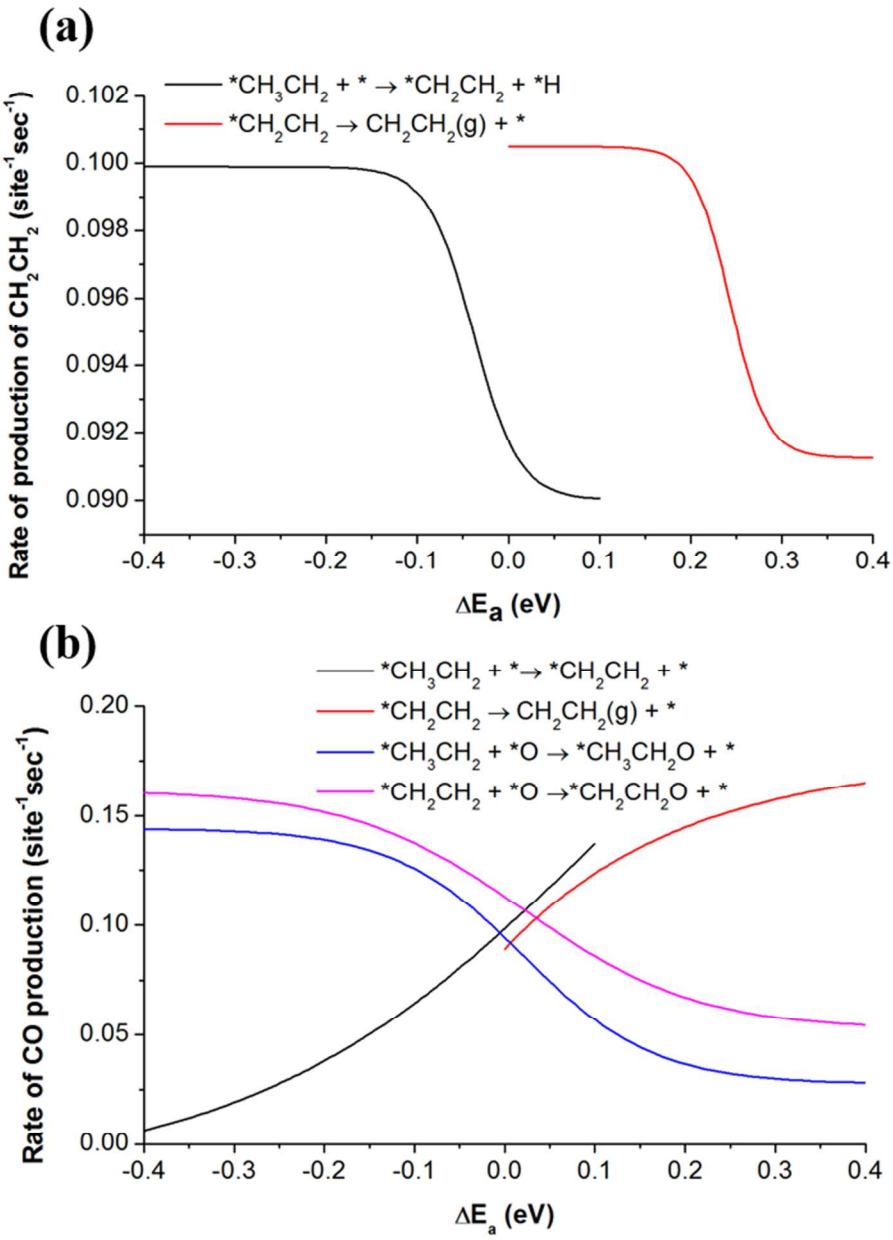

Figure 10. Sensitivity of CH_2CH_2 and CO production during CH_3CH_3 dry reforming by CO_2. (a) CH_2CH_2 production to variation of E_a of $*CH_2CH_2 \rightarrow CH_2CH_2 + *$ and $*CH_3CH_2 + * \rightarrow *CH_2CH_2 + *H$, (b) CO production to variation of E_a of $*CH_3CH_2 + *O \rightarrow *CH_3CH_2O + *$, $*CH_2CH_2 \rightarrow CH_2CH_2 + *$, $*CH_2CH_2 + *O \rightarrow *CH_2CH_2O + *$ and $*CH_3CH_2 + * \rightarrow *CH_2CH_2 + *H$. In this case only CO produced from C-C bond scission of CH_3CH_3 was included, which contributes to the syngas production.

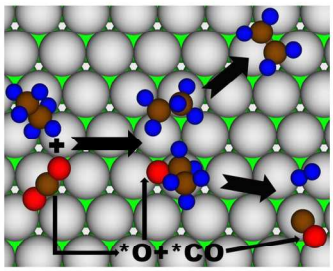

Combined DFT and KMC study pinpoints the origin of high selectivity toward syngas during CO_2 reduction by CH_3CH_3 on a PtNi model catalyst.

254x190mm (220 x 220 DPI)